ROYAL SOCIETY OF CHEMISTRY

EDGE ARTICLE

Check for updates

All publication charges for this article have been paid for by the Royal Society of Chemistry

Tuning reactivity at uranium through heterometal substitution in a redox-active thiomolybdate metalloligand

Leyla R. Valerio, Claire M. Dopp, William W. Brennessel [ID] and Ellen M. Matson [ID] *

Redox-active metalloligands are advantageous for their ability to serve as electron reservoirs to facilitate multielectron transformations at metal centers. However, strategies for tuning their electronic properties remain limited, and investigation into how these changes impact reactivity at the coordinated metal center is understudied, particularly in the field of actinide chemistry. Isolation of a heterometal-substituted uranium-bound thiomolybdate assembly was performed using a pre-assembled "UMo$_2$" complex, $Cp*_3(UI_2)Mo_2S_4$, which serves as a platform to synthesize the zirconium-substituted derivative, $(Cp*_3ZrMo_2S_4)Cp*UCl_2$. Further reduction affords the fully reduced cluster, $(Cp*_3ZrMo_2S_4)Cp*U$, which was used in comparative small molecule activation studies with its homometallic analogue, $(Cp*_3Mo_3S_4)Cp*U$. The reactivity of the fully reduced cluster with azobenzene was investigated, resulting in the formation a high-valent uranium bis-imido complex. Bond metric analysis of the Zr-doped species reveals that heterometal substitution forces localization of oxidation at the uranium center, generating a U^{VI}-bis(imido) species, $(Cp*_3ZrMo_2S_4)Cp*U(NPh)_2$. Addition of elemental sulfur to $(Cp*_3ZrMo_2S_4)Cp*U$ generates a unique disulfide-bridged product, $(Cp*_3ZrMo_2S_4)Cp*U(\mu_2-S_2)_2$. This contrasts with the reactivity of the all-molybdenum analogue and elemental sulfur which favors decomposition under analogous conditions. These results indicate that tuning the electronic structure of redox-active thiomolybdate metalloligands through heterometal substitution serves as an effective strategy for modulating multielectron reactivity at uranium.

Introduction

The development of chemical uses for long-lived radionuclides generated in the front-end enrichment of nuclear fuels (*e.g.* ^{238}U) provides a motivation to investigate the fundamental reactivity of the actinides. Indeed, uranium's ability to access a range of oxidation states (*e.g.* U(II), U(III), U(IV), U(V), U(VI)) has translated to its study in challenging multielectron molecular transformations.[1–6] The basis for the rich redox chemistry of uranium has been credited to the ability of 5f-orbitals to hybridize with 6d-orbitals, presenting opportunities for f-electrons to participate in bonding and reactivity.[7–12]

Studies have demonstrated that the reactivity of low-valent uranium complexes is dependent on the distribution of electron density between the metal and supporting ligand. Storing excess reducing equivalents (*i.e.*, electron density) on redox-active ligands can have profound effects on the electronic structure and reactivity of uranium complexes. Early examples include the arene-bridged diuranium complex, $(\mu-C_7H_8)[U(N[R]Ar)_2]_2$ (R = C(CH$_3$)$_3$, Ar = 3,5-C$_6$H$_3$Me$_2$), in which electron density stored in the bridging aromatic ring generates a formal

Department of Chemistry, University of Rochester, Rochester, NY 14627, USA. E-mail: matson@chem.rochester.edu

tetra-anionic toluene molecule sandwiched between two U(IV) centers.[13] Ephritikine and Andersen reported the synthesis of trivalent uranium complexes with redox-active bipyridine ligands, $Cp^R_2U(2,2'-bpy)$ ($Cp^R = Me_5C_5$ or $(Me_3C)_3C_5H_2$), where a radical is delocalized over the 2,2'-bipyridine moiety (Fig. 1).[14,15] Complexes of this type were later extended to low valent uranium centers supported by the bulky hydrotris(3,5-dimethylpyrazolyl)borate ligand (Tp*), used to synthesize $Tp*_2U(2,2'-bpy)$, a sterically encumbered U(III) complex that could perform diazene cleavage at the uranium center.[16] Later, Bart and coworkers utilized the pyridine diimine (PDI) ligand as a redox reservoir for uranium, forming $[Cp^RU(^{Mes}PDI^{Me})]_2$ ($Cp^R = Me_5C_5$ or PhC(CH$_3$)$_2$C$_5$H$_4$) complexes, whereby varying the substituents on the imido or cyclopentadienyl ligands and the steric properties of the redox-active ligand results in marked changes in reactivity at uranium.[17] By tuning the localization of electron density between uranium and the PDI ligand, a family of uranium bis(imido) complexes with distinct electronic structures were isolated. In this context, understanding how uranium's electronic structure and reactivity is affected by redox-active ligands is key to developing design principles for cooperative activation of small molecule substrates.

As an alternative approach to using redox-active ligands based on organic scaffolds, a growing number of frameworks
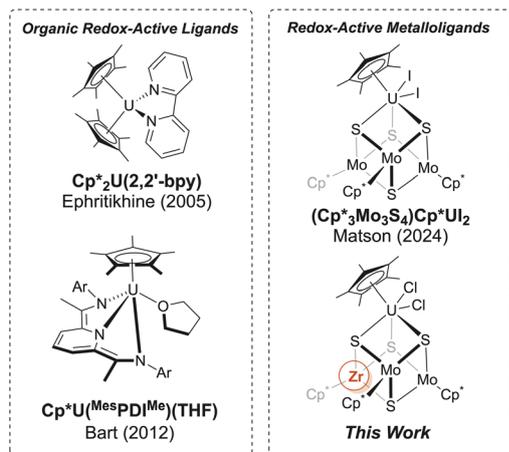
Fig. 1 Selected complexes featuring organic redox-active ligands and inorganic redox-active metalloligands.

composed of redox-active metalloligands have been reported (Fig. 1).[18–20] These ligands retain the favorable properties inherent to organic redox-active ligands, namely the ability to serve as electron reservoirs for multiple-electron transformations, while also benefiting from stronger electronic coupling to the host metal, unique spin states and valence distributions, and three-dimensional molecular structures.[21–23] Ohki and coworkers have found that the anionic thiomolybdate cluster, $[Cp^*_3Mo_3S_4]^{1-}$ ($Cp^* = Me_5C_5$), acts as a metalloligand for transition metals; the titanium derivative, $(Cp^*_3Mo_3S_4)TiCl_2$, activates N_2 upon treatment with potassium graphite (KC_8), to form the N_2-bridged product.[24,25] Interested in extending this methodology to actinides, our group is investigating (Cp^*_3-Mo_3S_4) as a redox-active metalloligand for uranium. The addition of the low-valent uranium precursor, $Cp^*UI_2(thf)_3$, to ($Cp^*_3Mo_3S_4$), followed by reduction, results in the formation of a uranium-substituted thiomolybdate cluster, ($Cp^*_3Mo_3S_4$)Cp^*U, that displays cooperative redox-behavior for small molecule activation.[26–28]

To date, strategies used to tune the redox properties of metalloligands have largely focused on modifying the supporting ligands. For example, it has been demonstrated that substitution of ancillary cyclopentadienide ligands has subtle effects on the reduction potential of trimolybdenum tetrasulfide hemicube clusters; indeed, modification of the steric and electron donating properties of the ligands translate to distinct reactivities of reduced, iron-appended derivatives of the title compounds with N_2.[29] However, an unexplored approach to modifying the electronic structure of metalloligands involves heterometal substitution. This concept is well-established for modifying the reactivity of cluster complexes and extended materials, but to date has not been invoked for modulating the electronic properties of redox-active metalloligands.[30,31] Recently, our lab has shown that substitution of a cobalt atom for molybdenum in $Cp^*_3Mo_3S_4$ has drastic effects on the electronic properties of the cluster.[32] Inspired by this result, we sought to investigate how heterometal substitution in Cp^*_3-Mo_3S_4 would influence the electronic structure of the uranium-

bound cluster, as well as modulate the reactivity of the actinide-substituted cluster with small molecule substrates.

Here, we report the synthesis of a heterometal-substituted thiomolybdate uranium complex. The target complexes were synthesized *via* a uranium-substituted precursor, **$Cp^*_3(UI_2)$ Mo_2S_4**; introduction of a Zr(IV) center results in the isolation of the heterometallic actinide-substituted cluster, **($Cp^*_3ZrMo_2S_4$) Cp^*UCl_2**. Reduction of the assembly yields the low-valent species, **($Cp^*_3ZrMo_2S_4$)Cp^*U**. The reactivity of the reduced species was investigated and compared to that of its homometallic analogue, ($Cp^*_3Mo_3S_4$)Cp^*U. Substitution of Zr for Mo within the thiomolybdate framework imparts changes in the electronic structure and redox behavior of the uranium-substituted complex, where incorporation of Zr has a significant impact on the oxidation state distribution and reactivity at uranium. Treatment of **($Cp^*_3ZrMo_2S_4$)Cp^*U** with azobenzene results in the formation of the U(VI) *cis-bis*(imido) product, with oxidation localized at the uranium center. Similarly, reaction of **($Cp^*_3ZrMo_2S_4$)Cp^*U** with elemental sulfur generates a novel disulfide-bridged product. This is accompanied by significant structural changes in the metalloligand. Collectively, our findings demonstrate that heterometal substitution within the redox-active thiomolybdate framework serves as an effective strategy for tuning uranium-centered reactivity in multimetallic systems.

Experimental

General considerations

All air- and moisture sensitive manipulations were carried out using standard high vacuum line, Schlenk, or cannula techniques, or in an MBraun inert atmosphere drybox containing an atmosphere of purified dinitrogen. Solvents for air- and moisture-sensitive manipulations were dried and deoxygenated using a Glass Contour Solvent Purification System (Pure Process Technology, LLC) and stored over activated 4 Å molecular sieves (Fisher Scientific) prior to use. Deuterated solvents for ^1H NMR spectroscopy were purchased from Cambridge Isotope Laboratories and stored in the glovebox over activated 3 Å molecular sieves after three freeze-pump-thaw cycles. Chemicals were purchased from commercial sources (Sigma Aldrich, Fisher-Scientific) and used without further purification. *Syn*-Cp^*_2-Mo_2S_4, $Cp^*UI_2(thf)_3$, KC_8, ($Cp^*_3Mo_3S_4$), and ($Cp^*_3Mo_3S_4$)Cp^*UI_2 were synthesized following established procedures.[24,26,33–35]

Safety considerations

Caution! depleted uranium (primary isotope ^{238}U) is a weak α-emitter (4.197 MeV) with a half-life of 4.47×10^9 years; manipulations and reactions should be carried out in monitored fume hoods or in an inert atmosphere drybox in a radiation laboratory equipped with α- and β-counting equipment.

Synthesis of $[K(Cp^*_3ZrMo_2S_4)]_2$

In a glovebox, a 20 mL scintillation vial was charged with *syn*-$Cp^*_2Mo_2S_4$ (0.03 g, 0.051 mmol) and 5 mL of tetrahydrofuran (THF). The solution was shaken vigorously to ensure dissolution

of the solid and then placed in the freezer for ten minutes to cool to −30 °C. The solution was then added to a vial of KC$_8$ (0.007 g, 0.051 mmol) equipped with a magnetic stir bar and allowed to stir for 30 seconds. In a separate vial, Cp*ZrCl$_3$ (0.017 g, 0.051 mmol) in 3 mL THF was also cooled to −30 °C and added to the previous vial dropwise. After an additional 30 seconds of stirring, the reaction mixture was added to a vial charged with three additional equivalents of KC$_8$ (0.021 g, 0.155 mmol) and the solution was allowed to stir for one hour. The reaction mixture was filtered over a bed of Celite with a glass microfiber plug and the solvent was removed under reduced pressure. The solid was then extracted into toluene, filtered over Celite, and dried under reduced pressure. The product was washed with pentane and dried in vacuo to afford the title compound. Yield: 0.03 g, 0.035 mmol, 70%. ^{1}H NMR (400 MHz, C$_6$D$_6$): δ = 2.50 (s, 15H, Cp*Zr–H), 1.95 (s, 30H, Cp*Mo–H). Brown crystals suitable for single-crystal X-ray diffraction were grown from a concentrated solution of the product in benzene at room temperature. Anal. Calcd. for C$_{60}$H$_{90}$K$_2$Zr$_2$Mo$_4$S$_8$·0.5C$_6$H$_6$ (mol. wt. 1712.305 g mol^{-1}): C, 43.21%; H, 5.35%; N, 0%. Found: C, 43.311%; H, 5.287%; N, 0.177%.

Synthesis of Cp*$_3$(UI$_2$)Mo$_2$S$_4$

In a glovebox, a 20 mL scintillation vial was charged with syn-Cp*$_2$Mo$_2$S$_4$ (0.05 g, 0.085 mmol) dissolved in toluene (∼8 mL). One equivalent of Cp*UI$_2$(THF)$_3$ (0.072 g, 0.085 mmol) was added to the vial as a solid and gently swirled, resulting in an immediate color-change of the solution to dark brown. The solution was filtered over a bed of Celite with a glass microfiber plug and the solvent was removed in vacuo. The solid was washed with pentane to afford crystalline product. Yield = 0.10 g, 0.082 mmol, 96%. ^{1}H NMR (400 MHz, C$_6$D$_6$): δ = 4.02 (s, 15H, Cp*U–H), 2.78 (s, 30H, Cp*Mo–H). Brown crystals suitable for single-crystal X-ray diffraction were grown from a concentrated solution of the product in benzene at room temperature. Anal. Calcd. for C$_{30}$H$_{45}$S$_4$Mo$_2$UI$_2$·0.3C$_6$H$_6$ (mol. wt. 1217.304 g mol^{-1}): C, 30.78%; H, 3.8%; N, 0%. Found: C, 31.089%; H, 3.719%; N, −0.259%.

Synthesis of (Cp*$_3$ZrMo$_2$S$_4$)Cp*UCl$_2$

In a glovebox, a 20 mL scintillation vial was charged with Cp*$_3$(UI$_2$)Mo$_2$S$_4$ (0.06 g, 0.049 mmol) dissolved in toluene (∼5 mL). Cp*ZrCl$_3$ (0.016 g, 0.049 mmol) was weighed out into a second vial and dissolved in toluene (∼3 mL). The solution of Cp*ZrCl$_3$ was added to the first vial and the reaction mixture was swirled gently. In a third scintillation vial equipped with a stir bar, potassium graphite (KC$_8$; 0.033 g, 0.247 mmol) was weighed out and set to stir. The reaction mixture was added to the vial of powdered KC$_8$ and allowed to stir for one hour. The solution was filtered over a bed of Celite with a glass microfiber plug and the solvent was removed under reduced pressure. The solid was washed with pentane to afford crystalline product. Yield = 0.052 g, 0.041 mmol, 84%. ^{1}H NMR (400 MHz, C$_6$D$_6$): δ = 9.09 (s, 15H, Cp*U–H), 1.78 (s, 30H, Cp*Mo–H), and 0.28 (s, 15H, Cp*Zr–H). Red-brown crystals suitable for single-crystal X-

ray diffraction were grown from a concentrated solution of the product in toluene at room temperature. Anal. Calcd. for C$_{40}$H$_{60}$S$_4$Mo$_2$ZrUCl$_2$·0.1C$_7$H$_8$ (mol. wt. 1261.213 g mol^{-1}): C, 38.48%; H, 4.82%; N, 0%. Found: C, 38.524%; H, 4.779%; N, −0.013%.

Synthesis of (Cp*$_3$ZrMo$_2$S$_4$)Cp*U

The title compound can be prepared through two approaches:

Method A. In a glovebox, a 20 mL scintillation vial was charged with (Cp*$_3$ZrMo$_2$S$_4$)Cp*UCl$_2$ (0.045 g, 0.036 mmol) dissolved in toluene (∼10 mL). Potassium graphite (KC$_8$; 0.019 g, 0.143 mmol) was weighed into a vial equipped with a stir bar, and the toluene solution was added to the powdered KC$_8$. The reaction mixture was allowed to stir for 16 hours, after which the solution was filtered over a bed of Celite with a glass microfiber plug. The solvent was removed under reduced pressure to afford the title compound as a black powder. Yield = 0.022 g, 0.018 mmol, 52%.

Method B. In a glovebox, a 20 mL scintillation vial equipped with a stir bar was charged with (Cp*$_3$ZrMo$_2$S$_4$)Cp*UCl$_2$ (0.060 g, 0.048 mmol) dissolved in toluene (∼10 mL). Sodium napthalenide (0.374 M in THF, 0.32 mL, 0.119 mmol) was added and the solution was allowed to stir for 15 minutes. The reaction mixture was filtered over a bed of Celite with a glass microfiber plug, and the solvent was removed under reduced pressure to afford the title compound as a black powder. Yield = 0.043 g, 0.036 mmol, 75%.

^{1}H NMR (400 MHz, C$_6$D$_6$) δ −0.48 (s, 30H, Cp*Mo–H), −4.49 (s, 15H, Cp*Zr–H), and −6.12 (s, 15H, Cp*U–H). Anal. Calcd. for C$_{40}$H$_{60}$S$_4$Mo$_2$ZrU·0.5C$_7$H$_8$ (mol. wt. 1236.383 g mol^{-1}): C, 42.26%; H, 5.22%; N, 0%. Found: C, 42.216%; H, 5.001%; N, 0.235%.

Synthesis of (Cp*$_3$ZrMo$_2$S$_4$)Cp*U(NPh)$_2$

In a glovebox, a 20 mL scintillation vial was charged with (Cp*$_3$ZrMo$_2$S$_4$)Cp*U (0.020 g, 0.017 mmol) dissolved in 3 mL of toluene. In a separate vial, azobenzene (0.003 g, 0.017 mmol) was dissolved in 2 mL of toluene. The azobenzene solution was added dropwise to the solution of (Cp*$_3$ZrMo$_2$S$_4$)Cp*U and gently swirled upon complete addition. The solvent was immediately removed under reduced pressure. The resultant solid was washed with pentane and subsequently dried in vacuo, affording the title compound as a dark crystalline solid. Yield = 0.016 g, 0.012 mmol, 70%. ^{1}H NMR (400 MHz, C$_6$D$_6$): δ = 9.21 (s, 4H, NPh–H), 5.41 (s, 15H, Cp*U–H), 3.95 (d, J = 7.9 Hz, 4H, NPh–H), 2.31 (s, 15H, Cp*Zr–H), 2.06 (t, J = 7.4 Hz, 2H, NPh–H), 1.69 (s, 30H, Cp*Mo–H). Crystals suitable for single crystal X-ray diffraction were grown from a concentrated toluene solution of the title compound at −30 °C. Anal. Calcd for C$_{52}$H$_{70}$S$_4$ZrMo$_2$UN$_2$·0.2KCl (mol. Wt. 1521.636): C, 45.02%; H, 5.09%; N, 2.02%. Found: C, 44.826%; H, 5.084%; N, 1.842%.

Synthesis of (Cp*$_3$ZrMo$_2$S$_4$)Cp*U(μ_2-S$_2$)$_2$

In a glovebox, a 20 mL scintillation vial was charged with (Cp*$_3$ZrMo$_2$S$_4$)Cp*U (0.020 g, 0.017 mmol) dissolved in 3 mL of toluene. In a separate vial, sulfur (0.002 g, 0.008 mmol) was

dissolved in 2 mL of toluene. Both solutions were cooled to −30 °C for ten minutes. The sulfur solution was added to the solution of (Cp*$_3$ZrMo$_2$S$_4$)Cp*U and gently swirled after addition. The solution was filtered, and the solvent was removed under reduced pressure. The solid was washed with pentane and subsequently dried *in vacuo*, affording the title compound as a dark crystalline solid. Yield = 0.016 g, 0.012 mmol, 73%. ^{1}H NMR (400 MHz, C$_7$H$_8$): δ = 11.69 (s, 15H, Cp*U–H), 0.52 (s, 30H, Cp*Mo–H), −1.74 (s, 15H, Cp*Zr–H). Crystals suitable for single crystal X-ray diffraction were grown from a concentrated toluene solution of the title compound at −30 °C. Anal. Calcd. for C$_{40}$H$_{60}$S$_8$ZrMo$_2$U (mol. wt. 1318.533 g mol^{-1}): C, 43.38%; H, 5.39%; N, 0%. Found: C, 43.311%; H, 5.287%; N, 0.177%.

Physical measurements

^{1}H NMR spectra were recorded at room temperature on a 400 MHz or 500 MHz Bruker AVANCE spectrometer locked on the signal of deuterated solvents. All the chemical shifts are reported relative to the chosen deuterated solvent as a standard. Elemental analysis data were obtained from the Elemental Analysis Facility at the University of Rochester. Microanalysis samples were weighed with a PerkinElmer model AD6000 Autobalance and their compositions were determined with a PerkinElmer 2400 Series II analyzer. Air-sensitive samples were handled in a VAC Atmospheres glovebox. Cyclic voltammetry experiments were performed using a three-electrode setup inside a nitrogen filled glove box (MBraun UniLab, USA) using a Bio-Logic SP 150 potentiostat/galvanostat and the EC-Lab software suite. The concentration of the analyte and the supporting electrolyte (tetrabutylammonium tetrakis(3,5-bis(trifluoromethyl)phenylborate, TBABArF$_{24}$; tetrabutylammonium hexafluorophosphate, TBAPF$_6$) were kept at 1 mM and 100 mM, respectively, throughout all measurements. Cyclic voltammograms were recorded using a 3 mm diameter glassy carbon working electrode (CH Instruments, USA), a Pt wire auxiliary electrode (CH Instruments, USA), and a Ag wire reference electrode (CH Instruments, USA). Ferrocene (Fc) was added as an internal standard after the completion of the measurements, and all potentials were referenced *versus* the Fc$^+$/Fc^0 couple. All cyclic voltammogram experiments were *iR* compensated at 85% with impedance taken at 100 kHz using the ZIR tool included within the EC-Lab software.

X-ray crystallography

Each single crystal was collected on a nylon loop and mounted on a Rigaku XtaLAB Synergy-S Dualflex diffractometer equipped with a HyPix-6000HE HPC area detector for data collection at 100.00(10) K. A preliminary set of cell constants and an orientation matrix were calculated from a small sampling of reflections. A short pre-experiment was run, from which an optimal data collection strategy was determined. The full data collection was carried out using a PhotonJet (Cu) X-ray source for complexes **[K(Cp*$_3$ZrMo$_2$S$_4$)]$_2$, (Cp*$_3$ZrMo$_2$S$_4$)Cp*UCl$_2$, (Cp*$_3$-ZrMo$_2$S$_4$)Cp*U(NPh)$_2$,** and **(Cp*$_3$ZrMo$_2$S$_4$)Cp*U(μ_2-S$_2$)$_2$,** while analysis of crystals of **Cp*$_3$(UI$_2$)Mo$_2$S$_4$** was performed using a Photon Jet (Mo) X-ray source. After the intensity data were

corrected for absorption, the final cell constants were calculated from the xyz centroids of the strong reflections from the actual data collections after integration. The structure was solved using SHELXT[36] and refined using SHELXL.[37] Most or all non-hydrogen atoms were assigned from the solution. Full-matrix least-squares/difference Fourier cycles were performed, which located any remaining non-hydrogen atoms. All of the non-hydrogen atoms were refined with anisotropic displacement parameters. All of the hydrogen atoms were placed in ideal positions and refined as riding atoms with relative isotropic displacement parameters.

Results and discussion

Varying electronic properties of redox-active metalloligands

Interested in modulating the ground state electronic structure of low-valent uranium complexes supported by redox-active thiomolybdate metalloligands, we considered molecular modifications that would tune the physicochemical properties of the parent cluster. We hypothesized that to decouple changes in electronic structure and the sterics of the ligand framework we could generate heterometal-substituted hemicuboidal thiomolybdate clusters of the general formula Cp*$_3$MMo$_2$S$_4$. Our initial work focused on zirconium as a heterometal dopant for the thiomolybdate assembly. Our interest in this metal stemmed from its proximity to Mo on the periodic table (both are second-row transition metals). This point results in identical ionic radii for the tetravalent ions (Zr(IV) = 0.79 Å; Mo(IV) = 0.79 Å),[38] suggesting successful substitution of a single Mo center for Zr would not perturb the molecular structure of the complex. However, Zr is more electropositive than Mo and is more difficult to reduce, factors that we hypothesized would influence the electronic properties of the assembly.

Synthesis of the Zr-substituted thiomolybdate cluster was accomplished *via* addition of Cp*ZrCl$_3$ and excess reductant to *syn*-Cp*$_2$Mo$_2$S$_4$ (Scheme 1), in analogy to procedures recently reported by our team for the formation of Cp*$_3$CoMo$_2$S$_4$.[32] Following work-up, the product was characterized by ^{1}H NMR spectroscopy; two signals located at 2.50 and 1.95 ppm are observed, integrating in a 1 : 2 ratio, respectively (Fig. S1). The ^{1}H NMR spectrum is consistent with that predicted for the desired product. A small amount of the homometallic cluster, Cp*$_3$Mo$_3$S$_4$ is observed at ~8.5 ppm; this impurity is challenging to separate from the desired product and is observed in all attempts to synthesize the Zr-doped assembly.
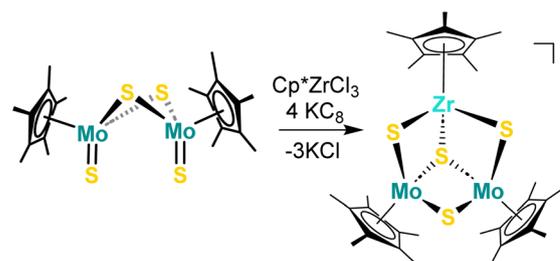
Scheme 1 Synthesis of [K(Cp*$_3$ZrMo$_2$S$_4$)]$_2$.
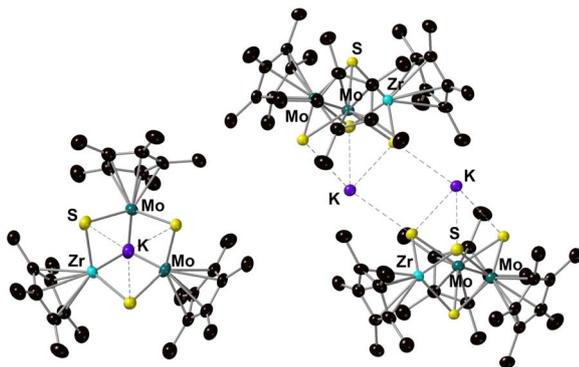
Fig. 2 Molecular structure of $[K(Cp^*_3ZrMo_2S_4)]_2$ shown with 30% probability ellipsoids. Hydrogen atoms and co-crystallized solvent molecules have been removed for clarity. The full molecular structure of the dimer is shown on the right, while a perspective of the Zr-doped thiomolybdate core is shown on the left.

To confirm formation of the target Zr-substituted thiomolybdate cluster, single crystals of the product of the reaction of Cp^*ZrCl_3 and syn-$Cp^*_2Mo_2S_4$ were analyzed by single crystal X-ray diffraction (SCXRD). Refinement of the data reveals successful formation of the target complex in its reduced, dimeric form, $[K(Cp^*_3ZrMo_2S_4)]_2$ (Fig. 2, Table 1, Fig. S2, and Table S1). Incorporation of the Zr dopant into the thiomolybdate assembly is accomplished via coordination of two terminal sulfido ligands and a bridging sulfido moiety of the molybdenum starting material to the heterometal center. We note that all chloride ligands have been removed from Zr by the reductant, resulting in a coordination environment saturated by the η^5-Cp^* ligand and three bridging sulfido moieties. The asymmetric unit of $[K(Cp^*_3ZrMo_2S_4)]_2$ is composed of the $ZrMo_2$ core, with bridging sulfide groups capped by a potassium ion.

Comparison of bond metrics of $[K(Cp^*_3ZrMo_2S_4)]_2$ to those reported for the reduced homometallic cluster, $[K(18-C-6)Cp^*_3Mo_3S_4]$ (18-C-6 = 1,4,7,10,13,16-hexaoxacyclooctadecane), is valuable for understanding the structural impact(s) of Zr-substitution.[24] Notably, the Zr-substituted assembly crystallizes as a dimer, where each associated potassium ion bridges two clusters through contacts with facial sulfide ions. The K–S bond

distances to sulfido ligands coordinated also to Zr (3.063(2), 3.079(2) Å) are shorter than the value observed for the K–S contact to the μ_2-S^{2-}-moiety featuring only interactions with Mo (3.152(2) Å). This observation suggests that the presence of a heterometal dopant increases the basicity of adjacent sulfido sites, biasing the interactions of the cation to one side of the cluster. In contrast, the potassium cation of $[K(18-C-6)Cp^*_3Mo_3S_4]$ symmetrically caps the face of the hemicuboidal assembly, interacting with all three sulfide atoms and its 18-crown-6 ligand.

Structural data provides opportunities to make inferences related to oxidation state distributions in cluster complexes, as variations in bond lengths and coordination geometries are typically sensitive to changes in electron density at specific metal centers. Perturbations of M–S bonds upon incorporation of the Zr-substituent are modest; this observation is consistent with the fact that the ionic radii of Zr- and Mo- are identical.[38] The Mo–S bonds of $[K(Cp^*_3ZrMo_2S_4)]_2$ are slightly longer (Mo–S_{avg} = 2.376(1) Å) than similar metrics reported for $[K(18-C-6)Cp^*_3Mo_3S_4]$ (Mo–S_{avg} = 2.343(1) Å). Additionally, the Mo–Mo distance in $[K(Cp^*_3ZrMo_2S_4)]_2$ of 2.825(7) Å is slightly shorter than that observed in $[K(18-C-6)Cp^*_3Mo_3S_4]$ (Mo–Mo = 2.853(4)–2.857(4) Å).[24] Collectively these data suggest the molybdenum centers are more reduced in the heterometal-substituted assembly as compared to its homometallic congener. Given the more negative reduction potential of the Zr dopant, one would expect reduction of the assembly to be localized at the two molybdenum centers of the cluster, resulting in an oxidation state distribution of metal ions in $[K(Cp^*_3ZrMo_2S_4)]_2$ of $Zr(IV)Mo(III)_2$.

To assess electronic differences between the Zr-substituted and homometallic thiomolybdate clusters, both complexes were characterized by cyclic voltammetry. The cyclic voltammogram (CV) of $[K(Cp^*_3ZrMo_2S_4)]_2$, measured in tetrahydrofuran (THF) with tetrabutylammonium tetrakis(3,5-bis(trifluoromethyl) phenyl)borate, $(TBABArF_{24})$ as the supporting electrolyte, is shown in Fig. 3. The Zr-substituted cluster exhibits two reversible redox processes (Fig. S3) with $E_{1/2}$ values of −1.48 and −0.74 V ($vs.$ $Fc^{+/0}$; Table S2). An open circuit potential (OCP) for $[K(Cp^*_3ZrMo_2S_4)]_2$ is measured at −1.54 V, indicating that the observed redox processes are likely Mo-based oxidations, and that the anionic, Zr-doped thiomolybdate cluster is isolated in its most reduced charge state. The observed redox chemistry of $[K(Cp^*_3ZrMo_2S_4)]_2$ is quite different from that of its homometallic analogue, $Cp^*_3Mo_3S_4$ ($E_{1/2}$ = −2.32 and −1.33 V $vs.$ $Fc^{+/0}$), which possesses two reversible redox processes that are shifted cathodically by nearly 1 V relative to $[K(Cp^*_3ZrMo_2S_4)]_2$. While shifts to more positive potentials upon installation of a more Lewis acidic metal center is precedented,[39,40] the magnitude of the observed shift is striking. Additionally, the separation between redox events in $[K(Cp^*_3ZrMo_2S_4)]_2$ ($\Delta E_{1/2}$ = 0.74 V) is much smaller than that of $Cp^*_3Mo_3S_4$ ($\Delta E_{1/2}$ = 0.99 V), translating to comproportionation constants (K_c) of 3.39×10^{12} ($[K(Cp^*_3ZrMo_2S_4)]_2$) and 6.02×10^{16} ($Cp^*_3Mo_3S_4$). This change is consistent with a decrease in the extent of delocalization of electron density across the thiometalate assembly upon heterometal substitution.[41,42] Similarly, the redox chemistry of $[K(Cp^*_3ZrMo_2S_4)]_2$ compared to syn-
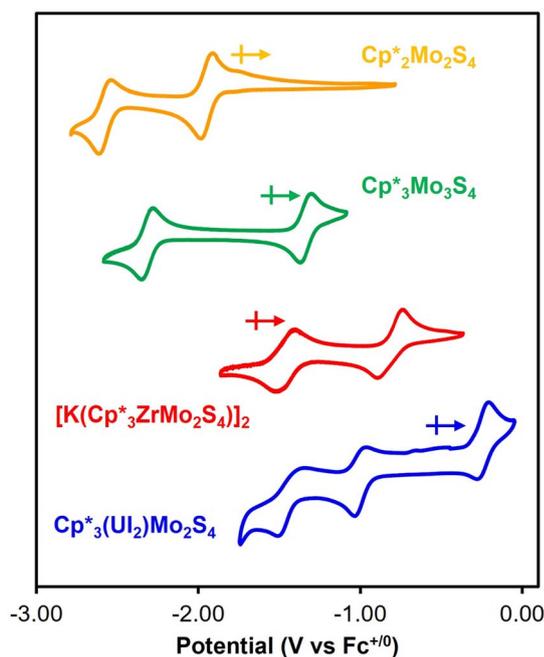
Table 1 Selected bond lengths (Å) of [(Cp*$_3$Mo$_3$S$_4$)(K-18C6)] and [K(Cp*$_3$ZrMo$_2$S$_4$)]$_2$

Bond	[K(18-C-6)Cp*Mo$_3$S$_4$]	[KCp*$_3$ZrMo$_2$S$_4$]$_2$
Zr–(μ_2-S_{Mo})	—	2.397(2), 2.439(12)
Zr–(μ_3-S)	—	2.403(1)
Zr–C(Cp*)$_{avg}$	—	2.478(6)
Mo–Mo	2.853(4), 2.856(4), 2.857(4)	2.825(7)
Mo–(μ_3-S)	2.342(9), 2.344(9), 2.344(8)	2.3679(14), 2.3835(13)
Mo–(μ_2-S_{Zr})	—	2.402(2), 2.412(2)
Mo–(μ_2-S_{Mo})	2.339(9), 2.346(1)	2.3432(3), 2.357(1)
Mo–C(Cp*)$_{avg}$	2.374 (avg)	2.391 (avg)

Fig. 3 Cyclic voltammograms of $Cp^*_2Mo_2S_4$ (orange trace), Cp^*_3-Mo_3S_4 (green trace), $[K(Cp^*_3ZrMo_2S_4)]_2$ (red trace) and $Cp^*_3(UI_2)$ Mo_2S_4 (blue trace). Data was acquired in THF with 0.1 M TBABArF$_{24}$ as the supporting electrolyte. And a scan rate of 200 mV s^{-1}. Potential values are expressed with reference to the ferrocenium/ferrocene redox couple ($Fc^{+/0}$).

$Cp^*_2Mo_2S_4$ reveals pronounced differences between the complexes. The CV of syn-$Cp^*_2Mo_2S_4$ possesses two redox events (-2.57 V and -1.94 V $vs.$ $Fc^{+/0}$ in THF), assigned to sequential reductions of the dimeric species ($Mo(v)_2 \rightarrow Mo(iv)_2$). Incorporation of the Lewis acidic Zr(iv) center into the Mo_2S_4 framework induces a distinct anodic shift of the Mo-based events, attributed to strong inductive effects operating through the sulfur-bridges. The electropositive Zr(iv) ion draws electron density from the Mo centers in $[K(Cp^*_3ZrMo_2S_4)]_2$, stabilizing these events and resulting in the drastic shifts in the CV of the Zr-substituted cluster compared to the homometallic complexes.

Synthesis of uranium complexes with heterobimetallic redox-active metalloligands

Upon successful formation of the Zr-substituted thiomolybdate, we turned our attention to its reactivity with low-valent

uranium. In prior work, our team described formation of a uranium-capped thiomolybdate, $(Cp^*_3Mo_3S_4)Cp^*UI_2$, via addition of $(Cp^*_3Mo_3S_4)$ to $Cp^*UI_2(thf)_3$.[26] We note that formation of the actinide-substituted assembly is driven by electron transfer from low-valent uranium to $(Cp^*_3Mo_3S_4)$.[43] Given the anodic shift in reduction potentials of the Zr-doped thiomolybdate cluster in comparison to its homometallic congener, we hypothesized that a similar preparatory pathway would result in successful formation of $(Cp^*_3ZrMo_2S_4)Cp^*UI_2$. However, addition of $[K(Cp^*_3ZrMo_2S_4)]_2$ to $Cp^*UI_2(thf)_3$ results in the formation of a complex mixture of products that could not be separated (Fig. S4).

Undeterred, we proposed an alternative synthetic pathway for the formation of the target complex. Rather than invoking coordination of low-valent uranium to a pre-formed hetero-metallic thiomolybdate assembly, we hypothesized that initial coordination of the actinide center to the molybdenum sulfide dimer, syn-$Cp^*_2Mo_2S_4$, would result in formation of a "UMo$_2$" complex that could be used as a ubiquitous precursor for generation of $(Cp^*_3MMo_2S_4)Cp^*UI_2$ complexes. Indeed, the CV of syn-$Cp^*_2Mo_2S_4$ displays two Mo(v) $\rightarrow$ Mo(iv) redox events (-2.57 V and -1.94 V $vs.$ $Fc^{+/0}$ in THF), suggesting that reduction of the assembly upon coordination of uranium would be possible (Fig. 3). Addition of $Cp^*UI_2(thf)_3$ to a toluene solution of syn-$Cp^*_2Mo_2S_4$ results in the dissolution of the semi-soluble starting materials and an immediate color change to dark brown (Scheme 2). Following work-up, the brown crystalline product was analyzed via ^1H NMR spectroscopy. The spectrum reveals two singlets at 4.02 and 2.78 ppm that integrate to a ratio of 1 : 2, respectively (Fig. 4 and S5). The resonance at 4.02 ppm is assigned to the Cp* ligand protons bound to the U center, and the higher intensity signal at 2.78 ppm corresponds to the Mo-bound Cp* ligand protons.

Structural analysis of $Cp^*_3(UI_2)Mo_2S_4$ was possible following refinement of data collected from SCXRD experiments (Fig. 5, and Tables 2, S3). Crystals suitable for analysis were grown from the slow evaporation of a concentrated solution of $Cp^*_3(UI_2)$ Mo_2S_4 in benzene at room temperature. The solid-state structure shows coordination of the uranium center to the molybdenum dimer through the terminal sulfide moieties and one of the bridging sulfide ligands. The U–I distances of $Cp^*_3(UI_2)$ Mo_2S_4 (3.039(2), 3.061(2) Å) are significantly shortened in comparison to $Cp^*UI_2(thf)_3$ (U–I = 3.161(1), 3.179(1) Å), resembling those previously reported for $(Cp^*_3Mo_3S_4)Cp^*UI_2$
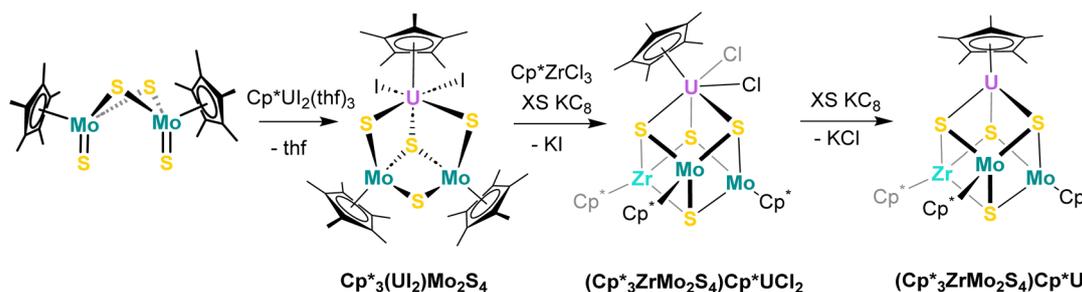
Scheme 2 Syntheses of $Cp^*_3(UI_2)Mo_2S_4$, $(Cp^*_3ZrMo_2S_4)Cp^*UCl_2$, and $(Cp^*_3ZrMo_2S_4)Cp^*U$.
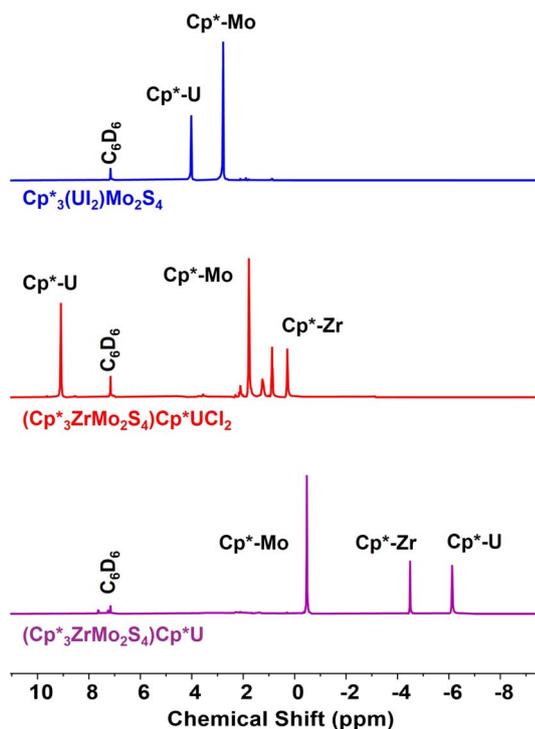
Fig. 4 ^{1}H NMR spectra of $\mathbf{Cp^*_3(UI_2)Mo_2S_4}$ (top), $\mathbf{(Cp^*_3ZrMo_2S_4)}$ $\mathbf{Cp^*UCl_2}$ (middle), and $\mathbf{(Cp^*_3ZrMo_2S_4)Cp^*U}$ (bottom) in C_6D_6 at room temperature.

Fig. 5 Molecular structures of $\mathbf{Cp^*_3(UI_2)Mo_2S_4}$ and $\mathbf{(Cp^*_3ZrMo_2S_4)}$ $\mathbf{Cp^*UCl_2}$ shown with 30% probability ellipsoids. Hydrogen atoms and co-crystallized solvent molecules have been removed for clarity.

(3.068(3), 3.083(3) Å) and other U(IV) complexes with iodide ligands (~3.06 Å).[26,44–47] This observation suggests that the U(III) starting material is oxidized to U(IV) upon coordination to *syn*-Cp*$_2$Mo$_2$S$_4$ (Table S4; structural data for this previously reported compound was collected, as data is missing from the Cambridge Structural Database). Reduction of the molybdenum assembly upon coordination of uranium is supported by the change in the Mo–Mo bond distance of the U-bound product, $\mathbf{Cp^*_3(UI_2)Mo_2S_4}$ (Mo–Mo = 2.846(1) Å) compared to *syn*-Cp*$_2$-Mo$_2$S$_4$ (Mo–Mo = 2.877(4) Å).[20,48] Incorporation of U into the framework additionally leads to more drastic perturbations of the Mo–S bonds compared to Zr-substitution in $\mathbf{[K(Cp^*_3\text{-}}$ $\mathbf{ZrMo_2S_4)]_2}$; significantly shorter bonds are observed for $\mathbf{Cp^*_3(UI_2)Mo_2S_4}$ (Mo-μ_2-S$_U$ = ~2.24 Å) than $\mathbf{[K(Cp^*_3ZrMo_2S_4)]_2}$ (Mo-μ_2-S$_{Zr}$ = ~2.41 Å). Collectively, the structural data suggests a formal oxidation state distribution of Mo(V)Mo(IV)U(IV) in $\mathbf{Cp^*_3(UI_2)Mo_2S_4}$.

To probe electronic effects resulting from U incorporation into the thiomolybdate cluster, $\mathbf{Cp^*_3(UI_2)Mo_2S_4}$ was characterized by cyclic voltammetry (Fig. 2 and Table S2).[49,50] The CV of $\mathbf{Cp^*_3(UI_2)Mo_2S_4}$ possesses two quasi-reversible reduction events with $E_{1/2}$ values of −1.44 V and −0.98 V (*vs.* Fc$^{+/0}$) and a quasi-reversible oxidation event with an $E_{1/2}$ value of −0.23 V (*vs.* Fc$^{+/0}$). Assuming a formal oxidation state distribution of Mo(V) Mo(IV)U(IV) in $\mathbf{Cp^*_3(UI_2)Mo_2S_4}$, the oxidative process is assigned to a Mo-based oxidation (Mo(IV) → Mo(V)) and the reductive event at −0.98 V (*vs.* Fc$^{+/0}$) is assigned to a Mo-based reduction (Mo(V) → Mo(IV)). The more negative reduction process at −1.44 V (*vs.* Fc$^{+/0}$) is attributed to the U(IV)/(III) redox couple.

Reported values for U(IV)/(III) redox couples vary widely in the literature, appearing anywhere between −0.61 V to −3.10 V (*vs.* Fc$^{+/0}$).[51] However, the measured potential of −1.44 V (*vs.* Fc$^{+/0}$) for $\mathbf{Cp^*_3(UI_2)Mo_2S_4}$ closely matches that of the U(IV)/(III) couple for (Cp^{iPr4})$_2$UI$_2$ in THF (−1.41 V *vs.* Fc$^{+/0}$).[52] Comparison of the CV of $\mathbf{Cp^*_3(UI_2)Mo_2S_4}$ to that of Cp*$_3$Mo$_3$S$_4$ and $\mathbf{[K(Cp^*_3\text{-}}$ $\mathbf{ZrMo_2S_4)]_2}$ reveals that incorporation of the redox-active U center into the thiomolybdate framework expands the accessible redox chemistry by providing access to an additional metal-based redox couple. The comproportionation constant (7.32×10^{11}) of the Mo-based redox events $(\Delta E_{1/2} = 0.70$ V) of $\mathbf{Cp^*_3(UI_2)Mo_2S_4}$ suggests a further decrease in the delocalization of electron density upon formation of the mixed uranium/molybdenum trimetallic assembly.[53]

With $\mathbf{Cp^*_3(UI_2)Mo_2S_4}$ in hand, we next targeted formation of the Zr-substituted assembly. Addition of Cp*ZrCl$_3$ to a toluene solution of $\mathbf{Cp^*_3(UI_2)Mo_2S_4}$ and excess KC$_8$ results in the formation of a new product (Scheme 2). Following work-up, analysis by ^{1}H NMR spectroscopy reveals a spectrum with three paramagnetically shifted and broadened resonances ($\delta = 9.09$, 1.78, and 0.28 ppm), integrating in a 1 : 2 : 1 ratio, respectively (Fig. 4 and S6). The distribution of signals is consistent with successful incorporation of the "Cp*Zr" fragment into $\mathbf{Cp^*_3(UI_2)}$ $\mathbf{Mo_2S_4}$. The most intense resonance at 1.78 ppm is assigned to the protons of the Mo-bound Cp* ligands, which are chemically equivalent in solution. The up-field shift of the Cp*-Mo resonance indicates greater shielding of the protons, likely arising from increased electron density at the Mo sites upon

Table 2 Selected bond lengths (Å) of $\mathbf{Cp^*_3(UI_2)Mo_2S_4}$ and $\mathbf{(Cp^*_3\text{-}}$ $\mathbf{ZrMo_2S_4)Cp^*UCl_2}$

Bond	$\mathbf{Cp^*_3(UI_2)Mo_2S_4}$	$\mathbf{(Cp^*_3ZrMo_2S_4)Cp^*UCl_2}$
U–X (Cl, I)	3.039(2), 3.061(2)	2.624(3), 2.721(5)
U–S	2.676(5), 2.716(6), 2.789(5)	2.809(1), 2.811(1), 2.816(1)
U–S$_{surf}$	—	1.899(9)
Mo–S$_U$	2.235(6), 2.255(6)	2.372(1), 2.371(1)
Mo–S$_{Mo}$ (avg)	2.311	2.343
Mo–S$_{Zr}$ (avg)	—	2.397
Zr–S$_U$	—	2.465(1), 2.475(1)
Zr–S$_{Mo}$	—	2.433(1)
Mo–Mo	2.846(4)	2.749(5)

incorporation of Zr into the framework. The resonance at 9.09 ppm is tentatively attributed to the Cp* ligand bound to the U center, while the remaining signal at 0.28 ppm is assigned to the Cp* ligand coordinated to Zr. These assignments are made by comparison of the chemical shifts to ^{1}H NMR spectra of other Zr- and U-doped assemblies reported in this work.

Red-brown crystals of the product suitable for X-ray analysis were grown from a concentrated toluene solution of the bulk material at room temperature (Fig. 5 and Tables 2, S5). The molecular structure confirms successful incorporation of Zr into the assembly, with the product identified as **(Cp*$_3$ZrMo$_2$S$_4$)Cp*UCl$_2$**. The uranium center is coordinated by a η^5-Cp* ligand, three sulfide ions from the thiomolybdate cluster, and two chloride ions. The chloride ligands are proposed to originate from halide transfer from Cp*ZrCl$_3$. The U–S bond distances in **(Cp*$_3$ZrMo$_2$S$_4$)Cp*UCl$_2$** (avg. = 2.812(1) Å) are slightly longer than those observed for the homometallic uranium cluster, (Cp*$_3$Mo$_3$S$_4$)Cp*UI$_2$ (avg. = 2.775(1) Å), indicating that substitution of Zr into the thiomolybdate assembly results in weaker interactions between uranium and the redox-active metalloligand.[26] This observation is further supported by examining the distance between the centroid defining the plane of three μ^2-bridged sulfur centers of the cluster and the U center; the U–S$_{surf}$ distance in **(Cp*$_3$ZrMo$_2$S$_4$)Cp*UCl$_2$** is 1.899(9) Å, longer than that in (Cp*$_3$Mo$_3$S$_4$)Cp*UI$_2$ (U–S$_{surf}$ = 1.856(8) Å).[26]

Additional perturbations in the cluster core are observed upon Zr-substitution. As expected, the Mo centers are more reduced in **(Cp*$_3$ZrMo$_2$S$_4$)Cp*UCl$_2$**, represented by a Mo–Mo bond distance of 2.749(5) Å, relative to that in (Cp*$_3$Mo$_3$S$_4$)Cp*UI$_2$ (Mo–Mo$_{avg}$ = 2.877(4) Å). Shorter Mo–S bond distances (Mo–S$_{Mo}$ = 2.343(1) Å) compared to the Zr–S bonds (Zr–S$_{Mo}$ 2.433(1) Å) further support localization of reduction to the Mo sites upon incorporation of Zr. Collectively, structural analysis suggests a formal oxidation state distribution of Mo(III)$_2$Zr(IV)U(IV) in **(Cp*$_3$ZrMo$_2$S$_4$)Cp*UCl$_2$**.

To determine how Zr-incorporation affects the redox properties of the uranium-bound clusters, CVs of **(Cp*$_3$ZrMo$_2$S$_4$)Cp*UCl$_2$** and (Cp*$_3$Mo$_3$S$_4$)Cp*UI$_2$ were collected (Fig. S7). The CV of **(Cp*$_3$ZrMo$_2$S$_4$)Cp*UCl$_2$** in THF with TBABArF$_{24}$ as the supporting electrolyte reveals a quasi-reversible reductive event with an $E_{1/2}$ value of −1.56 V (*vs.* Fc$^{+/0}$) and a quasi-reversible oxidative event with an $E_{1/2}$ value of −0.205 V (*vs.* Fc$^{+/0}$). Comparatively, the CV of **(Cp*$_3$Mo$_3$S$_4$)Cp*UI$_2$** in THF with TBABArF$_{24}$ as the supporting electrolyte exhibits multiple redox events that suggest cluster instability under the electrochemical conditions. Despite multiple attempts to improve the quality of the CV by product recrystallization and modification of experiment conditions, similar results were obtained. However, in the case of (Cp*$_3$Mo$_3$S$_4$)Cp*UI$_2$, we found that the complex can be reproducibly reduced to cleanly generate the iodide-free species, (Cp*$_3$Mo$_3$S$_4$)Cp*U. Therefore, we opted to move forward with comparative investigations of the reduction chemistry of **(Cp*$_3$ZrMo$_2$S$_4$)Cp*UCl$_2$**.

Treatment of **(Cp*$_3$ZrMo$_2$S$_4$)Cp*UCl$_2$** with an excess of KC$_8$ affords the fully reduced complex, **(Cp*$_3$ZrMo$_2$S$_4$)Cp*U** (Scheme 2). Characterization of the isolated product by ^{1}H NMR spectroscopy reveals three signals at −0.48, −4.49, and −6.12 ppm

in a 2 : 1 : 1 ratio, corresponding to the Cp* ligands on Mo, Zr, and U, respectively (Fig. 4 and S8). Assignment of the resonances associated with the Cp* ligands of Zr and U are inferred based on the expected larger paramagnetic pseudo-contact contribution and high degree of spin–orbit coupling anticipated for a paramagnetic uranium center, yielding the most upfield signal. Notably, there is a prominent up-field shift observed for all resonances in **(Cp*$_3$ZrMo$_2$S$_4$)Cp*U** relative to those in the ^{1}H NMR spectrum of **(Cp*$_3$ZrMo$_2$S$_4$)Cp*UCl$_2$**. This is indicative of greater shielding of the Cp* protons, consistent with increased electron density in the reduced species.

Comparison of the ^{1}H NMR spectrum of **(Cp*$_3$ZrMo$_2$S$_4$)Cp*U** with that of its homometallic congener, (Cp*$_3$Mo$_3$S$_4$)Cp*U, provides insights into oxidation state distribution within the Zr-substituted cluster (Fig. S9). The previously reported ^{1}H NMR spectrum of (Cp*$_3$Mo$_3$S$_4$)Cp*U displays paramagnetically shifted signals in a 3 : 1 ratio at −0.43 and −7.86 ppm, corresponding to the Cp* protons on Mo and U, respectively. The observed shifts in the ^{1}H NMR spectrum are consistent with a proposed oxidation state distribution of Mo(III)$_3$U(III) in the reduced compound. Notably, the resonance assigned to the Cp* protons bound to Mo is nearly identical between the two complexes (**(Cp*$_3$ZrMo$_2$S$_4$)Cp*U** = −0.48 ppm; (Cp*$_3$Mo$_3$S$_4$)Cp*U = −0.43 ppm), suggesting that the Mo atoms in the heterometallic cluster are in similar electronic environments despite incorporation of Zr into the framework. This data suggests the same number of electrons have been stored in the cluster.

There are several potential oxidation state distributions in **(Cp*$_3$ZrMo$_2$S$_4$)Cp*U**. Based on the similarities of chemical shifts of Cp*-Mo and Cp*-U protons in the ^{1}H NMR spectra of **(Cp*$_3$ZrMo$_2$S$_4$)Cp*U** and (Cp*$_3$Mo$_3$S$_4$)Cp*U, we tentatively assign the oxidation states of these metals as Mo(III) and U(III). The assignment of Mo(III) centers and a U(III) center in **(Cp*$_3$ZrMo$_2$S$_4$)Cp*U** necessitates a Zr(III) oxidation state to maintain charge balance. Although molecular Zr(III) complexes are quite rare, those that have been isolated rely on strongly donating Cp- and silyl-based ligands to help stabilize the low-valent metal center.[54–57] Combination of the strongly donating Cp* ligands and potential delocalization of electron density within **(Cp*$_3$ZrMo$_2$S$_4$)Cp*U** makes an assignment of a Zr(III) center reasonable. It is also possible that Zr(IV) retains its initial oxidation state with a U(II) center to provide a formal oxidation state distribution of Mo(III)$_2$Zr(IV)U(II). This outcome is plausible if the electropositive Zr(IV) ion forces reduction to be localized at uranium in **(Cp*$_3$ZrMo$_2$S$_4$)Cp*U**. Reduction could additionally occur at both uranium and molybdenum to give Mo(II)Mo(III)Zr(IV)U(III). Unfortunately, attempts to crystallize **(Cp*$_3$ZrMo$_2$S$_4$)Cp*U** for bond metric analysis have been unsuccessful. Additional spectroscopic and computational experiments are underway to confirm the oxidation state distribution for **(Cp*$_3$ZrMo$_2$S$_4$)Cp*U**.

Comparative investigations of the reactivity of low-valent uranium complexes supported by homo- and hetero-metallic redox-active metalloligands

Our initial motivation for synthesizing heterometallic thiomolybdate clusters was to modulate the electronic properties of
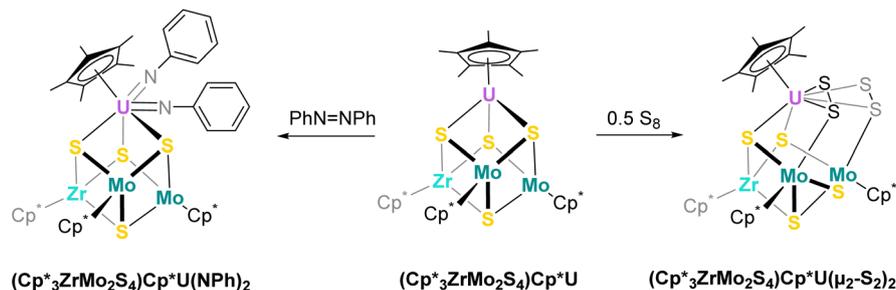
Scheme 3 Synthesis of (Cp*$_3$ZrMo$_2$S$_4$)Cp*U(NPh)$_2$ and (Cp*$_3$ZrMo$_2$S$_4$)Cp*U(μ$_2$-S$_2$)$_2$ from (Cp*$_3$ZrMo$_2$S$_4$)Cp*U.

the redox-active metalloligand, with the goal of understanding how these modifications influence the coordination and small molecule activation reactivity at the actinide center. Uranium complexes are well known to perform the reductive cleavage of diazenes, leveraging electron density stored both at the uranium center and redox-active ligand scaffolds for the 4e$^-$ reduction of the substrate.[16,58–61] Previous work from our group has shown that the homometallic uranium-bound cluster (Cp*$_3$Mo$_3$S$_4$)Cp*U is a potent reductant, capable of facilitating the 4e$^-$ activation of the N═N bond in azobenzene.[26] Interested in comparing reactivity at the uranium center of the homometallic cluster to our heterometallic cluster, we first investigated the reactivity of (Cp*$_3$ZrMo$_2$S$_4$)Cp*U with azobenzene (Scheme 3).

Addition of one equivalent of azobenzene to (Cp*$_3$ZrMo$_2$S$_4$)Cp*U in a J. Young NMR tube results in complete consumption of the starting material and quantitative formation of a single product, as evidenced by ^{1}H NMR spectroscopy (Fig. S10). The spectrum of the product displays three resonances corresponding to the Cp* ligand protons bound to Mo (1.69 ppm, 30H), Zr (2.31 ppm, 15H), and U (5.41 ppm, 15H), all shifted down-field from those of (Cp*$_3$ZrMo$_2$S$_4$)Cp*U. These down-field shifts are consistent with oxidation of the cluster following its reaction with azobenzene. Three additional resonances are identified at 2.06 (2H), 3.95 (4H), and 9.21 (4H) ppm, and are assigned to the protons on the phenylimido substituents bound to the uranium center following azobenzene activation.

Crystals suitable for SCXRD were grown from a concentrated toluene solution of the product at −30 °C. Refinement of the

data confirms formation of the anticipated product, (Cp*$_3$-ZrMo$_2$S$_4$)Cp*U(NPh)$_2$ (Fig. 6, and Table 3, S6), revealing complete N═N bond cleavage and installation of two phenyl-imido substituents at the uranium center. Generally speaking, the structure of the bis-imido product is very similar to that of its homometallic congener. The general structural similarities between the two complexes allow for in-depth bond metric analysis to distinguish systematic changes arising from Zr-incorporation into the framework. The imido ligands adopt a *cis*-geometry (<= 98.43(14)°) with U–N bond lengths (1.977(3) and 1.993(3) Å) in the range of other reported high-valent U(v) and U(vi) imido species (1.90–2.20 Å).[62–67] The U–S bond distances in (Cp*$_3$ZrMo$_2$S$_4$)Cp*U(NPh)$_2$ (avg. = 2.888 Å) are longer than those observed for (Cp*$_3$ZrMo$_2$S$_4$)Cp*UCl$_2$ (avg. = 2.775 Å), consistent with oxidation of the uranium center. Cluster oxidation is further supported by a significant increase in the U–S$_{surf}$ distance of (Cp*$_3$ZrMo$_2$S$_4$)Cp*U(NPh)$_2$ (U–S$_{surf}$ = 1.995(5) Å) compared to (Cp*$_3$ZrMo$_2$S$_4$)Cp*UCl$_2$ (U–S$_{surf}$ = 1.897(9) Å).

Comparison of the bond metrics for (Cp*$_3$ZrMo$_2$S$_4$)Cp*U(NPh)$_2$ and (Cp*$_3$Mo$_3$S$_4$)Cp*U(NPh)$_2$ provides insight into the differing oxidation state distributions between the hetero-metallic and homometallic uranium clusters. Contrary to the uranium-imido species formed from oxidation of (Cp*$_3$Mo$_3$S$_4$)Cp*U with azobenzene, where the uranium center is proposed to undergo oxidation from U(iii) to U(v), the bond metric parameters of (Cp*$_3$ZrMo$_2$S$_4$)Cp*U(NPh)$_2$ suggest a more oxidized uranium center (*e.g.*, U(vi)). Indeed, shorter U═N bond
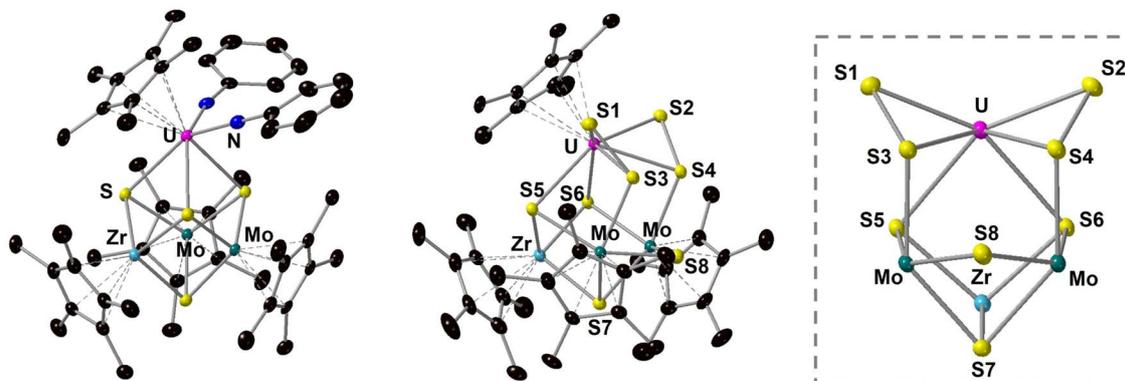
Fig. 6 Molecular structures of (Cp*$_3$ZrMo$_2$S$_4$)Cp*U(NPh)$_2$ and (Cp*$_3$ZrMo$_2$S$_4$)Cp*U(μ$_2$-S$_2$)$_2$ shown with 30% probability ellipsoids. Hydrogen atoms and co-crystallized solvent molecules have been removed for clarity.

Table 3 Selected bond lengths (Å) of $(Cp^*_3ZrMo_2S_4)Cp^*U(NPh)_2$ and $(Cp^*_3ZrMo_2S_4)Cp^*U(\mu_2\text{-}S_2)_2$

Bond	$(Cp^*_3ZrMo_2S_4)Cp^*U(NPh)_2$	$(Cp^*_3Mo_3S_4)Cp^*U(NPh)_2$	$(Cp^*_3ZrMo_2S_4)Cp^*U(\mu_2\text{-}S_2)_2$
Mo–Mo	2.737(4)	2.771(1), 2.932(1), 2.889(1)	3.190(7)
Mo–S_{Mo}	2.343(7)	2.362(3), 2.326(3), 2.331(3), 2.347(3), 2.364(3), 2.349(3)	2.440(2), 2.361(2), 2.447(2), 2.364(2)
Mo–S (S_2^{2-})	—	—	2.487(2), 2.478(2)
Mo–Zr	3.048(3), 3.059(3)	—	3.284(7), 3.263(8)
Zr–S_U	2.463(7), 2.456(7)	—	2.430(2), 2.422(2)
U–S	2.831(7), 2.885(7), 2.949(7)	2.771(2), 2.896(3), 2.989(3)	2.821(2), 2.843(2)
U–C_{avg}	2.757	2.788	2.776
U–Cp^*_{cent}	2.502(1)	2.511(5)	2.501(3)
U–S (S_2^{2-})	—	—	2.739(2), 2.652(2), 2.737(2), 2.651(2)
S–S (S_2^{2-})	—	—	2.066(2)
U–N	1.977(3), 1.993(3)	2.024(8), 2.015(9)	—

lengths are observed for the **$(Cp^*_3ZrMo_2S_4)Cp^*U(NPh)_2$** (1.977(3) and 1.993(3) Å) in comparison to those for $(Cp^*_3Mo_3S_4)Cp^*U(NPh)_2$ (2.024(8) and 2.015(9) Å). The U=N distances in **$(Cp^*_3ZrMo_2S_4)Cp^*U(NPh)_2$** are more similar to U(VI)-imido complexes in the literature.[65,66,68–70] The U(VI) cis-(bis) imido complex, $Cp^*_2U(NPh)_2$, possesses a phenylimido distance of 1.952(7) Å, and the U(VI) complexes, $[(Me_3Si)_2N]_3$-U(NPh)F and $[U(BIPM^{TMS})(NMes)(O)(DMAP)_2]$ ($BIPM^{TMS}$ = $C(PPh_2NSiMe_3)_2$; Mes = $2,4,6\text{-}Me_3C_6H_2$; DMAP = 4-(dimethylamino)pyridine) have U=N distances of 1.979(8) Å and 1.921(2) Å, respectively.[65,69,70] Though reports of U(V)- and U(VI)-imido bond distances vary depending on the complex, the differences in bond metrics between **$(Cp^*_3ZrMo_2S_4)Cp^*U(NPh)_2$** and $(Cp^*_3Mo_3S_4)Cp^*U(NPh)_2$ provide strong evidence for oxidation more strongly localized at uranium in the Zr-substituted cluster.

We next explored the multielectron reactivity of **$(Cp^*_3ZrMo_2S_4)Cp^*U$** toward elemental sulfur (S_8). Sulfur activation is a well-established probe of oxidative atom-transfer chemistry at uranium; typical coordination modes involve bridging chalcogenido ligands between two uranium centers or monomeric disulfide complexes.[71–77] Upon treatment of **$(Cp^*_3ZrMo_2S_4)Cp^*U$** with 0.5 equiv. of S_8 in a J. Young NMR tube, a slight color change of the solution from green-brown to red-brown was observed. Analysis of the crude reaction mixture by ^{1}H NMR spectroscopy shows three paramagnetically shifted resonances at 11.69, 0.52, and −1.74 ppm, integrating in a 1 : 2 : 1 ratio, respectively (Fig. S11). The resonance at 0.52 ppm is attributed to the protons of the Cp* ligand bound to Mo, while the resonances at 11.69 ppm and −1.74 ppm are assigned to the Cp*-U and Cp*-Zr protons.

Elucidation of the identity of the product was performed by single crystal X-ray diffraction. Crystals grown from a concentrated toluene solution of the product at −30 °C reveals the solid-state structure of **$(Cp^*_3ZrMo_2S_4)Cp^*U(\mu_2\text{-}S_2)_2$** (Fig. 6 and Table 3, S7), in which the coordination environment of the uranium center is composed of the η^5-Cp* ligand, two sulfide donors from the Zr-containing edge of the metalloligand, and two η^2-bound S_2^{2-} moieties. The U–S bonds of the disulfide ligands are

asymmetric, with U–S1 and U–S2 bond distances of 2.652(2) and 2.651(2) Å, and longer U–S3 and U–S4 distances of 2.739(2) and 2.737(2) Å, respectively. The S–S distances are 2.066(2) Å, falling within the range of other reports of uranium–disulfide moieties.[71,72] The disparity in bond lengths of the disulfido ligand in **$(Cp^*_3ZrMo_2S_4)Cp^*U(\mu_2\text{-}S_2)_2$** can be attributed to the secondary interactions between the molybdenum atoms in the cluster framework and the sulfur atoms (S3 and S4) of the S_2^{2-} ligands.

Inspection of the molecular structure also reveals significant perturbations to the thiomolybdate framework upon sulfur activation at the uranium center. Rather than the typical three μ-sulfide bridges to U observed in the parent cluster, only two are retained, both originating from the Zr-bound edge of the assembly. The Zr–S_U bond distances are 2.422(2) and 2.430(2) Å, shorter than those in **$(Cp^*_3ZrMo_2S_4)Cp^*UCl_2$** (2.465(1), 2.475(1) Å) and **$(Cp^*_3ZrMo_2S_4)Cp^*U(NPh)_2$** (2.463(7), 2.456(7) Å), suggesting stronger interactions between the sulfur atoms adjacent to zirconium and the uranium center following oxidation of the cluster. Distortions of the (Mo_2S_4) fragment are also apparent in the solid-state molecular structure. The bridging sulfur atom (S8) between the molybdenum centers does not interact with uranium and instead lies in-plane with the heterometal core. This is reflected in the S_{Mo}–Mo–S_{Zr} angle of 136.36(6)°, markedly larger than that for **$(Cp^*_3ZrMo_2S_4)Cp^*UCl_2$** (98.71(5)°).

The structure of **$(Cp^*_3ZrMo_2S_4)Cp^*U(\mu_2\text{-}S_2)_2$** is notable due to its distinct coordination environment compared to other reported disulfide uranium complexes. The secondary interactions between the S_2^{2-} moiety and Mo atoms of the cluster represent an uncommon structural feature in uranium coordination chemistry, though reports of this bonding motif are found in some multimetallic transition metal systems.[78,79] Hayton and coworkers have reported a structurally analogous motif in a bis–uranium complex supported by trimethylsilylamide ligands, where a bridging disulfide ($\mu\text{-}\eta^2{:}\eta^2$-$S_2$) ligand is present between the two uranium centers.[75] However, **$(Cp^*_3ZrMo_2S_4)Cp^*U(\mu_2\text{-}S_2)_2$** represents a unique case where the S_2^{2-} ligand exhibits both side-on and end-on coordination modes to distinct metal centers (U and Mo, respectively) in a discrete heterotrimetallic cluster.

In contrast to **(Cp*₃ZrMo₂S₄)Cp*U**, treatment of (Cp*₃Mo₃S₄)Cp*U with elemental sulfur results in decomposition of the cluster, as evidenced by a color change of the solution to green and the presence of free Cp*₃Mo₃S₄ metalloligand in the ^{1}H NMR spectrum of the crude reaction mixture (Fig. S12). The differing reactivity in these two systems highlights the influence of the cluster core composition on redox distribution within the framework, and subsequent reactivity at the uranium center. The increased nucleophilicity of the sulfido moieties coordinated to the Zr center likely strengthens interactions with uranium, helping to stabilize the cluster in the presence of elemental sulfur by biasing coordination to the doped face of the cluster. Moreover, replacement of a redox-active Mo site with Zr(ɪᴠ) in **(Cp*₃ZrMo₂S₄)Cp*U** preferences oxidation at uranium, enabling successful activation of S₈. In contrast, the delocalization of electron density and decreased basicity of the sulfur atoms in (Cp*₃Mo₃S₄)Cp*U destabilizes the cluster upon oxidation, leading to dissociation of uranium from the metalloligand.

Conclusion

We report a new method for accessing heterometal-doped thiomolybdate metalloligands, facilitated by the isolation of the molecular precursor, **Cp*₃(UI₂)Mo₂S₄**. Incorporation of Zr(ɪᴠ) into the uranium-bound framework generates the heterometallic species, **(Cp*₃ZrMo₂S₄)Cp*UCl₂**, which can be further reduced to form the low-valent complex, **(Cp*₃ZrMo₂S₄)Cp*U**. Comparison with the homometallic analogue, (Cp*₃Mo₃S₄)Cp*U, reveals that heterometal doping results in significant changes in the electronic and redox properties of the cluster. The electropositive nature of Zr(ɪᴠ) shifts electron density onto the Mo sites in the cluster, promoting oxidation localized at the uranium center. This is evidenced through the successful activation of elemental sulfur using **(Cp*₃ZrMo₂S₄)Cp*U**, where a stable disulfide-bridged product is isolated; comparatively, the all-molybdenum congener undergoes rapid decomposition under the same conditions.

Our findings reveal that tuning the electronic structure of redox-active thiomolybdate metalloligands through heterometal substitution is an effective strategy for modulating multielectron reactivity at uranium. Broadly, this work demonstrates how molybdenum sulfide complexes can serve as building blocks for designing actinide complexes with unique electronic structures and tailored reactivity. Ongoing investigations in our laboratory are focused on installing electron-rich heterometal dopants into the framework to determine effects on the electronic structure and redox-flexibility of the assembly.

Author contributions

L. R. V. synthesized and characterized all compounds. C. M. D. aided in synthesis at early stages of the project. W. W. B determined all crystal structures. E. M. M directed the project. The manuscript was written through contributions of all authors. All authors have given approval to the final version of the manuscript.

Conflicts of interest

There are no conflicts to declare.

Data availability

Acknowledgements

Notes and references

1 L. Barluzzi, S. R. Giblin, A. Mansikkamäki and R. A. Layfield, *J. Am. Chem. Soc.*, 2022, **144**, 18229–18233.

2 C. Deng, J. Liang, R. Sun, Y. Wang, P.-X. Fu, B.-W. Wang, S. Gao and W. Huang, *Nat. Commun.*, 2023, **14**, 4657.

3 H. Idriss, *Surf. Sci. Rep.*, 2010, **65**, 67–109.

4 M. Keener, R. A. K. Shivaraam, T. Rajeshkumar, M. Tricoire, R. Scopelliti, I. Zivkovic, A.-S. Chauvin, L. Maron and M. Mazzanti, *J. Am. Chem. Soc.*, 2023, **145**, 16271–16283.

5 E. Lu and S. T. Liddle, *Dalton Trans.*, 2015, **44**, 12924–12941.

6 J. Su, W.-L. Li, G. V. Lopez, T. Jian, G.-J. Cao, W.-L. Li, W. H. E. Schwarz, L.-S. Wang and J. Li, *J. Phys. Chem.*, 2016, **120**, 1084–1096.

7 M. L. Neidig, D. L. Clark and R. L. Martin, *Coord. Chem. Rev.*, 2013, **257**, 394–406.

8 B. M. Gardner, P. A. Cleaves, C. E. Kefalidis, J. Fang, L. Maron, W. Lewis, A. J. Blake and S. T. Liddle, *Chem. Sci.*, 2014, **5**, 2489–2497.

9 L. Zhang, G. Hou, G. Zi, W. Ding and M. D. Walter, *J. Am. Chem. Soc.*, 2016, **138**, 5130–5142.

10 S. T. Liddle, *Angew. Chem., Int. Ed.*, 2015, **54**, 8604–8641.

11 T. Vitova, I. Pidchenko, D. Fellhauer, P. S. Bagus, Y. Joly, T. Pruessmann, S. Bahl, E. Gonzalez-Robles, J. Rothe, M. Altmaier, M. A. Denecke and H. Geckeis, *Nat. Commun.*, 2017, **8**, 16053.

12 R. D. dos Reis, L. S. I. Veiga, C. A. Escanhoela, J. C. Lang, Y. Joly, F. G. Gandra, D. Haskel and N. M. Souza-Neto, *Nat. Commun.*, 2017, **8**, 1203.

13 P. L. Diaconescu, P. L. Arnold, T. A. Baker, D. J. Mindiola and C. C. Cummins, *J. Am. Chem. Soc.*, 2000, **122**, 6108–6109.

14 G. Zi, L. Jia, E. L. Werkema, M. D. Walter, J. P. Gottfriedsen and R. A. Andersen, *Organometallics*, 2005, **24**, 4251–4264.

15 T. Mehdoui, J.-C. Berthet, P. Thuéry, L. Salmon, E. Rivière and M. Ephritikhine, *Chem.–Eur. J.*, 2005, **11**, 6994–7006.

16 J. J. Kiernicki, R. F. Higgins, S. J. Kraft, M. Zeller, M. P. Shores and S. C. Bart, *Inorg. Chem.*, 2016, **55**, 11854–11866.

17 J. J. Kiernicki, M. G. Ferrier, J. S. Lezama Pacheco, H. S. La Pierre, B. W. Stein, M. Zeller, S. A. Kozimor and S. C. Bart, *J. Am. Chem. Soc.*, 2016, **138**, 13941–13951.

18 I. Takei, K. Suzuki, Y. Enta, K. Dohki, T. Suzuki, Y. Mizobe and M. Hidai, *Organometallics*, 2003, **22**, 1790–1792.

19 T. Auvray and E. M. Matson, *Dalton Trans.*, 2020, **49**, 13917–13927.

20 L. R. Valerio, K. Patra, D. Shiels, W. W. Brennessel and E. M. Matson, *Chem. Commun.*, 2025, **61**, 19660–19663.

21 D.-L. Long, E. Burkholder and L. Cronin, *Chem. Soc. Rev.*, 2007, **36**, 105–121.

22 H. Beinert, R. H. Holm and E. Münck, *Science*, 1997, **277**, 653–659.

23 S. C. Lee and R. H. Holm, *Angew Chem. Int. Ed. Engl.*, 1990, **29**, 840–856.

24 Y. Ohki, K. Uchida, R. Hara, M. Kachi, M. Fujisawa, M. Tada, Y. Sakai and W. M. C. Sameera, *Chem.–Eur. J.*, 2018, **24**, 17138–17147.

25 Y. Ohki, K. Uchida, M. Tada, R. E. Cramer, T. Ogura and T. Ohta, *Nat. Commun.*, 2018, **9**, 3200.

26 K. Patra, W. W. Brennessel and E. M. Matson, *Chem. Commun.*, 2024, **60**, 530–533.

27 K. Patra, W. W. Brennessel and E. M. Matson, *J. Am. Chem. Soc.*, 2024, **146**, 20147–20157.

28 K. Patra, W. W. Brennessel and E. M. Matson, *Dalton Trans.*, 2025, **54**, 966–976.

29 Y. Ohki, K. Munakata, Y. Matsuoka, R. Hara, M. Kachi, K. Uchida, M. Tada, R. E. Cramer, W. M. C. Sameera, T. Takayama, Y. Sakai, S. Kuriyama, Y. Nishibayashi and K. Tanifuji, *Nature*, 2022, **607**, 86–90.

30 J. Zhou, J. W. Raebiger, C. A. Crawford and R. H. Holm, *J. Am. Chem. Soc.*, 1997, **119**, 6242–6250.

31 R. Hernandez-Molina, M. N. Sokolov and A. G. Sykes, *Acc. Chem. Res.*, 2001, **34**, 223–230.

32 K. Patra, L. R. Valerio, Z. Lu, K. Kuphal, W. W. Brennessel and E. M. Matson, *J. Am. Chem. Soc.*, 2025, **147**, 38973–38978.

33 H. Brunner, W. Meier, J. Wachter, E. Guggolz, T. Zahn and M. L. Ziegler, *Organometallics*, 1982, **1**, 1107–1113.

34 L. R. Avens, C. J. Burns, R. J. Butcher, D. L. Clark, J. C. Gordon, A. R. Schake, B. L. Scott, J. G. Watkin and B. D. Zwick, *Organometallics*, 2000, **19**, 451–457.

35 S. Chakraborty, J. Chattopadhyay, W. Guo and W. E. Billups, *Angew. Chem., Int. Ed.*, 2007, **46**, 4486–4488.

36 G. Sheldrick, *Acta Crystallogr. A*, 2015, **71**, 3–8.

37 G. Sheldrick, *Acta Crystallogr. C*, 2015, **71**, 3–8.

38 R. D. Shannon, *Acta Crystallogr. A*, 1976, **32**, 751–767.

39 R. L. Meyer, W. W. Brennessel and E. M. Matson, *Polyhedron*, 2018, **156**, 303–311.

40 E. Y. Tsui and T. Agapie, *Proceedings of the National Academy of Sciences*, 2013, 110, 10084–10088.

41 M. A. Syzgantseva, C. P. Ireland, F. M. Ebrahim, B. Smit and O. A. Syzgantseva, *J. Am. Chem. Soc.*, 2019, **141**, 6271–6278.

42 L. E. VanGelder, W. W. Brennessel and E. M. Matson, *Dalton Trans.*, 2018, **47**, 3698–3704.

43 P. Miró and S. G. Duggan, *Dalton Trans.*, 2025, **54**, 8510–8517.

44 S. A. Pattenaude, C. S. Kuehner, W. L. Dorfner, E. J. Schelter, P. E. Fanwick and S. C. Bart, *Inorg. Chem.*, 2015, **54**, 6520–6527.

45 N. H. Anderson, S. O. Odoh, Y. Yao, U. J. Williams, B. A. Schaefer, J. J. Kiernicki, A. J. Lewis, M. D. Goshert, P. E. Fanwick, E. J. Schelter, J. R. Walensky, L. Gagliardi and S. C. Bart, *Nat. Chem.*, 2014, **6**, 919–926.

46 E. M. Matson, S. M. Franke, N. H. Anderson, T. D. Cook, P. E. Fanwick and S. C. Bart, *Organometallics*, 2014, **33**, 1964–1971.

47 M. J. Monreal, R. K. Thomson, T. Cantat, N. E. Travia, B. L. Scott and J. L. Kiplinger, *Organometallics*, 2011, **30**, 2031–2038.

48 Y.-C. Tsai, H.-Z. Chen, C.-C. Chang, J.-S. K. Yu, G.-H. Lee, Y. Wang and T.-S. Kuo, *J. Am. Chem. Soc.*, 2009, **131**, 12534–12535.

49 M. G. Hill, W. M. Lamanna and K. R. Mann, *Inorg. Chem.*, 1991, **30**, 4687–4690.

50 D. E. Morris, R. E. Da Re, K. C. Jantunen, I. Castro-Rodriguez and J. L. Kiplinger, *Organometallics*, 2004, **23**, 5142–5153.

51 J. Riedhammer, D. P. Halter and K. Meyer, *Chem. Rev.*, 2023, **123**, 7761–7781.

52 M. A. Boreen, D. J. Lussier, B. A. Skeel, T. D. Lohrey, F. A. Watt, D. K. Shuh, J. R. Long, S. Hohloch and J. Arnold, *Inorg. Chem.*, 2019, **58**, 16629–16641.

53 A. Hildebrandt, D. Miesel and H. Lang, *Coord. Chem. Rev.*, 2018, **371**, 56–66.

54 M. D. Fryzuk, L. Jafarpour and S. J. Rettig, *Organometallics*, 1999, **18**, 4050–4058.

55 E. J. Wimmer, S. V. Klostermann, M. Ringenberg, J. Kästner and D. P. Estes, *Eur. J. Inorg. Chem.*, 2023, **26**, e202200709.

56 O. Y. Lyakin, K. P. Bryliakov, V. N. Panchenko, N. V. Semikolenova, V. A. Zakharov and E. P. Talsi, *Macromol. Chem. Phys.*, 2007, **208**, 1168–1175.

57 S. J. Lancaster, in *Comprehensive Organometallic Chemistry III*, ed. D. M. P. Mingos and R. H. Crabtree, Elsevier, Oxford, 2007, pp. 741–757.

58 D. K. Modder, C. T. Palumbo, I. Douair, R. Scopelliti, L. Maron and M. Mazzanti, *Chem. Sci.*, 2021, **12**, 6153–6158.

59 E. M. Matson, P. E. Fanwick and S. C. Bart, *Eur. J. Inorg. Chem.*, 2012, **2012**, 5471–5478.

60 L. Maria, I. C. Santos, V. R. Sousa and J. Marçalo, *Inorg. Chem.*, 2015, **54**, 9115–9126.

61 D. P. Cladis, J. J. Kiernicki, P. E. Fanwick and S. C. Bart, *Chem. Commun.*, 2013, **49**, 4169–4171.

62 A. Zalkin, J. G. Brennan and R. A. Andersen, *Acta Crystallogr. C*, 1988, **44**, 1553–1554.

63 I. Castro-Rodriguez, K. Olsen, P. Gantzel and K. Meyer, *J. Am. Chem. Soc.*, 2003, **125**, 4565–4571.

64 B. P. Warner, B. L. Scott and C. J. Burns, *Angew. Chem., Int. Ed.*, 1998, **37**, 959–960.

65 D. S. J. Arney, C. J. Burns and D. C. Smith, *J. Am. Chem. Soc.*, 1992, **114**, 10068–10069.

66 D. S. J. Arney and C. J. Burns, *J. Am. Chem. Soc.*, 1995, **117**, 9448–9460.

67 S. C. Bart, C. Anthon, F. W. Heinemann, E. Bill, N. M. Edelstein and K. Meyer, *J. Am. Chem. Soc.*, 2008, **130**, 12536–12546.

68 L. P. Spencer, R. L. Gdula, T. W. Hayton, B. L. Scott and J. M. Boncella, *Chem. Commun.*, 2008, 4986–4988, DOI: 10.1039/B806075D.

69 C. J. Burns, W. H. Smith, J. C. Huffman and A. P. Sattelberger, *J. Am. Chem. Soc.*, 1990, **112**, 3237–3239.

70 E. Lu, O. J. Cooper, J. McMaster, F. Tuna, E. J. L. McInnes, W. Lewis, A. J. Blake and S. T. Liddle, *Angew. Chem., Int. Ed.*, 2014, **53**, 6696–6700.

71 S. M. Franke, F. W. Heinemann and K. Meyer, *Chem. Sci.*, 2014, **5**, 942–950.

72 J. K. Pagano, D. S. J. Arney, B. L. Scott, D. E. Morris, J. L. Kiplinger and C. J. Burns, *Dalton Trans.*, 2019, **48**, 50–57.

73 O. P. Lam, F. W. Heinemann and K. Meyer, *Chem. Sci.*, 2011, **2**, 1538–1547.

74 C. Camp, M. A. Antunes, G. García, I. Ciofini, I. C. Santos, J. Pécaut, M. Almeida, J. Marçalo and M. Mazzanti, *Chem. Sci.*, 2014, **5**, 841–846.

75 J. L. Brown, G. Wu and T. W. Hayton, *Organometallics*, 2013, **32**, 1193–1198.

76 D. E. Smiles, G. Wu and T. W. Hayton, *New J. Chem.*, 2015, **39**, 7563–7566.

77 E. M. Matson, M. D. Goshert, J. J. Kiernicki, B. S. Newell, P. E. Fanwick, M. P. Shores, J. R. Walensky and S. C. Bart, *Chem.–Eur. J.*, 2013, **19**, 16176–16180.

78 M. Rakowski DuBois, D. L. DuBois, M. C. VanDerveer and R. C. Haltiwanger, *Inorg. Chem.*, 1981, **20**, 3064–3071.

79 S. Yao, P. Hrobárik, F. Meier, R. Rudolph, E. Bill, E. Irran, M. Kaupp and M. Driess, *Chem.–Eur. J.*, 2013, **19**, 1246–1253.

80 (*a*) CCDC 2513355: Experimental Crystal Structure Determination, 2026, DOI: 10.5517/ccdc.csd.cc2qcbzf; (*b*) CCDC 2513356: Experimental Crystal Structure Determination, 2026, DOI: 10.5517/ccdc.csd.cc2qcc0h; (*c*) CCDC 2513357: Experimental Crystal Structure Determination, 2026, DOI: 10.5517/ccdc.csd.cc2qcc1j; (*d*) CCDC 2514132: Experimental Crystal Structure Determination, 2026, DOI: 10.5517/ccdc.csd.cc2qd51c; (*e*) CCDC 2514133: Experimental Crystal Structure Determination, 2026, DOI: 10.5517/ccdc.csd.cc2qd52d; (*f*) CCDC 2514134: Experimental Crystal Structure Determination, 2026, DOI: 10.5517/ccdc.csd.cc2qd53f.